Journal of Materials Research and Technology 28 (2024) 1611–1619

Contents lists available at ScienceDirect

Journal of Materials Research and Technology

journal homepage: www.elsevier.com/locate/jmrt

Development of Fe–Cr–Si deposited layer manufactured by laser directed energy deposition process

Gidong Kim [a,1], Hyunbin Nam [a,1], Taewoo Hwang [c], Seunghyun Kim [a], Ji Hyun Kim [b,*], Sangwoo Song [a,**]

[a] Department of Joining Technology, Korea Institute of Materials Science, Gyeongnam, 51508, South Korea
[b] Department of Nuclear Engineering, Ulsan National Institute of Science and Technology, Ulsan, 44919, South Korea
[c] Hydrogen Technology Research Team, Hyundai Steel, Chungnam, 31791, South Korea

ARTICLE INFO

Handling Editor: L Murr

Keywords:
Directed energy deposition
Fe–Cr–Si deposited layer
Corrosion behavior
High-temperature characteristics
Carbides
Phase transformation

ABSTRACT

In this study, the mechanical and corrosion characteristics of a corrosion-resistant layer made of stainless steel (STS) 316 L and Fe–Cr–Si alloy powder were investigated using laser-directed energy deposition (DED). In the STS 316 L deposited specimen, both the substrate and deposited layer were face-centred cubic (FCC). The deposited Fe–Cr–Si layer was clearly separated from the substrate because it was composed of body-centred cubic (BCC). Despite the phase differences, the surface of the Fe–Cr–Si-deposited layer showed a lower corrosion rate than that of the STS 316 L. All the deposited specimens exhibited typical high-temperature tensile behavior. However, the Fe–Cr–Si deposited layer at 600 °C showed a notable reduction in strength and increased elongation compared to the room temperature (RT) and 300 °C test results owing to the carbide concentration and phase transformation in the deposited layer. Because nuclear facilities mainly operate at temperatures below 600 °C, Fe–Cr–Si materials can also be used as nuclear piping coating materials. This study provides a mechanism for the high-temperature properties and corrosion resistance of the Fe–Cr–Si deposited layer and makes it competitive for application in fourth generation nuclear power systems.

1. Introduction

Most industrial plants are either petrochemical or nuclear plants, because thermoelectric power plants are required to operate in extreme environments, such as high temperatures and pressures, with corrosive media in contact, and corrosion and cracking or failures may occur in various pressure-retaining parts. In particular, nuclear power plant accidents occur owing to the corrosion behavior caused by immersion and exposure to high-temperature steam in pressurized water reactor (PWR) environments [1,2]. Therefore, it is important to determine the high-temperature characteristics and corrosion resistance of pressure-retaining materials [3–5].

Austenitic stainless steels (STSs) and heat-resistant alloys with excellent high-temperature characteristics and corrosion resistance are primarily used as piping materials that must withstand high temperatures [6–8]. When used in extreme environments, austenitic STS may deteriorate owing to the thermal deformation and oxidation [9–11]. Therefore, pressure retaining materials with excellent high-temperature properties are required.

Iron–chromium (Fe–Cr) alloys are major candidates for pressure-retaining materials because of their excellent creep strength, heat resistance, and corrosion resistance [12–15]. To apply Fe–Cr alloys as materials for nuclear applications, several studies have been conducted to analyse the mechanical and thermal properties of Fe–Cr alloys according to the Cr content [16,17]. The alloying elements mainly used in ultrahigh-strength steels are C, Mn, and Si. Among them, the Si component exhibits high solid solution strengthening and work hardening and effectively improves the strength and ductility by stabilising the retained austenite [18]. Furthermore, the addition of Si to the Fe–Cr alloy induces the segregation of Si at the grain boundaries of the alloy, which can significantly affect its final properties, such as corrosion and mechanical properties [19–21]. The Fe–Cr–Si alloy forms a multi-layer protective film (Iron–Oxide/Chromium Oxide/Silicon–Oxide), so it is used as a coating material candidate for PWR, primarily at high temperatures. In addition, the Fe–Cr–Si alloys are considered potential

* Corresponding author.
** Corresponding author.
E-mail addresses: kimjh@unist.ac.kr (J.H. Kim), swsong@kims.re.kr (S. Song).
[1] Gidong Kim and Hyunbin Nam contributed equally to this work.

https://doi.org/10.1016/j.jmrt.2023.12.029
Received 24 October 2023; Received in revised form 4 December 2023; Accepted 4 December 2023
Available online 12 December 2023

Nomenclature (abbreviations)

STS	Stainless steel
DED	Directed Energy Deposition
FCC	Face-centred cubic
BCC	Body-centred cubic
PWR	Pressurized water reactor
Fe–Cr	Iron-chromium
SMR	Small Modular Reactor
LBE	Lead-bismuth eutectic
CVD	Chemical vapor deposition
PVD	Physical vapor deposition
SEM	Scanning electron microscopy
BSE	backscattered electron
EBSD	Electron backscattered diffraction
IPF	Inverse pole figure
KAM	Kernel average misorientation
XRD	X-ray diffraction
EPMA	Electron probe microanalysis
OCP	Open-circuit potential
HAZ	Heat-affected zone
E_{corr}	Corrosion potential (mV)
I_{corr}	Corrosion current density (nA/cm^2)
RT	Room temperature
YS	Yield strength
TS	Tensile strength
E_f	Elongation (fracture)
QC	Quasi-cleavage

leaders as nuclear materials because they not only have excellent oxidation and creep resistance but also have low thermal neutron absorption capacity [22]. Many studies have been conducted on the high-temperature and corrosion properties of the Fe–Cr–Si alloys as nuclear materials [23–27]. In particular, small modular reactors (SMR) use lead-bismuth eutectic (LBE) as a coolant; therefore, the application of the Fe–Cr–Si alloy, which has excellent high-temperature corrosion resistance in the LBE environment, should be thoroughly considered. Previous studies have indicated that if the Si content of the Fe–Cr–Si alloys is lower than 1–1.2 wt%, they cannot have better corrosion resistance than the Fe–Cr alloys [22,28]. When the Si content of the Fe–Cr–Si alloys is higher than 2 wt%, they show excellent corrosion/oxidation resistance in LBE environments [29]. However, there are only few studies on improving the high-temperature and corrosion resistance by forming a functional layer using the Fe–Cr–Si powder. Among the various powder deposition technologies, additive manufacturing technology deposits the metal powder by irradiating a high-power laser and spraying the metal powder at the laser focus to melt the powder. It has the advantages of fast production speed and good product properties [30,31]. Unlike deposition technologies, such as chemical and physical vapor deposition (CVD/PVD), the deposited layers formed through additive manufacturing have excellent mechanical properties as no peeling or non-deposited areas are created.

This study investigates the high-temperature tensile properties and corrosion behavior of multilayer clads produced by laser DED using Fe–12Cr–2Si and STS 316 L powders. The mechanism of the high-temperature and corrosion characteristics is studied, and the applicability of the developed technology is presented.

2. Materials and methods

The diameters of the Fe–Cr–Si powder particles developed through gas atomisation, and the STS 316 L powder particles provided by Sandvik Osprey, were in the range 60–170 μm and 45–150 μm, respectively. The chemical compositions of the STS 316 L and Fe–Cr–Si powders used in this study are listed in Table 1. The STS 316 L was applied to the pipe; the nuclear materials were used as the substrates, which were Cr 16.9 wt%, Ni 11 wt%, Mo 2.8 wt%, Mn 1.5 wt%, Si 0.6 wt %, Al 0.02 wt% (Ti + C + O) 0.015 wt%, and balanced Fe. The STS 316 L and Fe–Cr–Si deposited specimens were fabricated using N1000 equipment (Makers & Solutions, Korea) equipped with a 1 kW diode-fibre laser system with laser diameter of 1.0 mm. The process parameters for the fabrication of the various deposited specimens were as follows: laser power 400 W, scanning speed 14 mm/s, powder feed rate 6 g/min, and hatch spacing 0.5 mm. This relatively low-heat-input process variable was selected to minimise Ni dilution from the substrate to deposited layer. This is because if the martensitic phase transformation was promoted by Ni dilution, the corrosion resistance of the Fe–Cr–Si deposited layer may have deteriorated. Two-layer cladding was produced using a zigzag hatch pattern. To prevent overheating, the second layer was deposited by rotating the deposition direction by 90° after the completion of the first layer, as shown in Fig. 1. The microstructural behaviours, hardness distributions, and corrosion properties of the two deposited specimens were investigated.

The macroscopic shapes of the two specimens deposited using the Fe–Cr–Si and STS 316 L powders were observed using the backscattered electron (BSE) mode of scanning electron microscopy (SEM). In addition, line and mapping analyses were performed using electron probe microanalysis (EPMA) to confirm the component behavior of each deposited specimen according to the powder type. The microstructure and phase transformation behavior of each deposited specimen were confirmed using inverse pole figures (IPF) and phase maps of electron backscattered diffraction (EBSD). X-ray diffraction (XRD) analysis was performed at a scan speed of 2°/min across a range of 20–90°, with a voltage of 40 kV and current of 30 mA using Cu Kα radiation to understand the detailed crystal structure of each deposited specimen.

To confirm the hardness distribution of each deposited specimen owing to the major microstructure types, the hardness was measured at intervals of 100 μm from the upper bead of the deposited layers to the substrate. The Vickers hardness was measured using a load of 200 gf (1.960 N) with 10 s loading cycles. A wide and thick multilayer deposited plate measuring 90 mm × 200 mm × 4 mm (t) was fabricated for the tensile test specimens of length 80 mm, width 20 mm, and thickness 1 mm, as shown in Fig. 2. It was essential to fabricate wide and thick deposited plates to verify the high-temperature (RT/300 °C/600 °C) tensile properties of the deposited plates manufactured using each powder (STS 316 L/Fe–Cr–Si). The tensile properties at each temperature were analysed based on a self-prepared tensile test specimen, and the tensile test was conducted at each temperature at a strain rate of 0.05 mm/s; the results are presented in Fig. 2. In addition, the deterioration mechanism of the high-temperature tensile behavior was identified through microstructural analysis near the fracture area, and the

Table 1
Chemical composition of stainless steel 316 L and Fe–Cr–Si powder used in this study.

Composition (wt.%)	Fe	Cr	Ni	Mo	Mn	Si	P	S	C
STS 316 L powder	Bal.	16.80	10.4	2.2	1.6	0.94	0.02	0.004	0.019
Fe–Cr–Si powder	Bal.	12.32	-	-	-	2.58	-	-	-

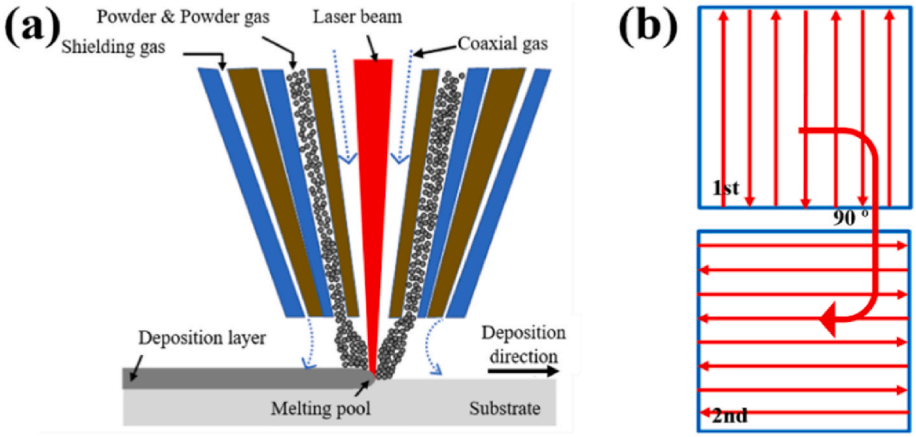

Fig. 1. (a) Schematics and (b) deposition method of laser direct energy deposition process.

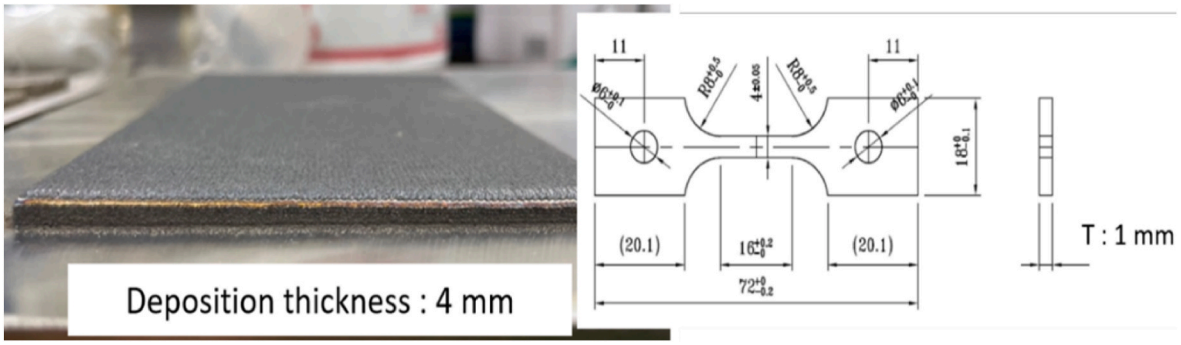

Fig. 2. Dimensions of prepared tensile test specimen.

correlation between the fracture shape and microstructure was confirmed through fracture analysis.

To characterise the general corrosion properties of each deposited layer, potentiodynamic polarisation experiments were performed using a Gamry Reference 600+ instrument. For the polarisation test, 0.5 M Na_2SO_4 was used as the electrolyte for the polarisation test. The cell was composed of three electrodes: multilayer clad of Fe–Cr–Si and STS 316 L, saturated KCl-filled Ag/AgCl as a reference electrode, and platinum mesh as a counter electrode. The experiments were conducted after 1 h of immersion in the test electrolyte, and the open-circuit potential (OCP) was measured to confirm the cell stability. Subsequently, a potentiostatic EIS was performed, and the polarisation test across the potential range of −0.5–1.5 V vs. OCP at a scan rate of 0.833 mV/s was performed.

3. Results and discussion

3.1. Microstructural and compositional behavior of each clad

Fig. 3 shows the melt-pool shapes of the deposited specimens produced using the STS 316 L and Fe–Cr–Si powders. Each deposited layer was fabricated by stacking two layers to observe the microstructural behavior of each specimen. Macro-defects, such as internal pores and cracks, were not observed in any of the specimens. However, because the melting temperature of the STS 316 L (1380 °C) is generally lower than that of the Fe–Cr–Si (1500 °C), it was confirmed that the thickness of the deposited layer using the STS 316 L powder was approximately ~100 μm thicker than that of the Fe–Cr–Si specimen. As shown in these results, the difference in the deposition thickness is related to the melting point of each powder, because the transfer rate and particle size of each powder are almost the same. Visual inspection revealed that coarse

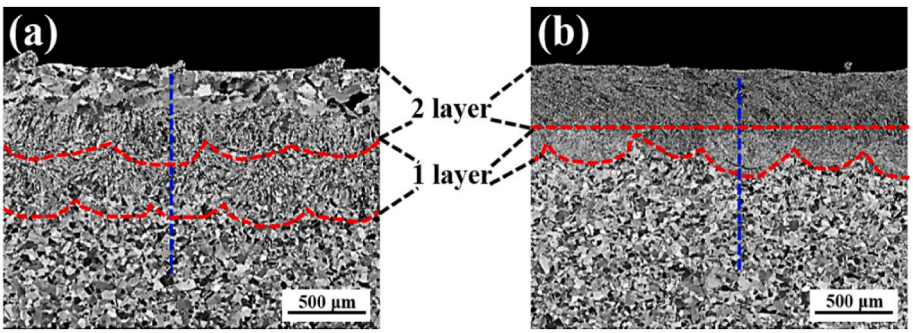

Fig. 3. Melt-pool shapes of deposited layers produced using: (a) stainless steel 316 L powder and (b) Fe–Cr–Si powder.

equiaxed grains were formed in the upper region of the STS 316 L s layer; coarse grains were not generated in the same region as the Fe–Cr–Si-deposited layer. This phenomenon may depend on the microstructure of each deposited layer. Later, the results of the microstructural behavior of the deposited specimen were analysed using EBSD. The interface between the substrate and deposited layer of the STS 316 L specimen was difficult to distinguish, whereas that of the Fe–Cr–Si specimen was easy to distinguish. This was because the composition of the STS 316 L powder was similar to that of the substrate, whereas the composition of the Fe–Cr–Si powder was different from that of the substrate, as shown in Table 1. This was because the major microstructures generated by the compositional differences in each deposited layer were different.

Fig. 4 shows the crystal structure acquired by XRD in the STS 316 L and Fe–Cr–Si deposited layers under the optimal conditions. The substrate was composed of a face-centred cubic (FCC) single phase with diffraction peaks ($2\theta = 43.5°$, 50.7°, and 74.6°). Through analysis of the XRD patterns, it was confirmed that the STS 316 L deposited layers were mainly composed of the FCC phase, whereas the Fe–Cr–Si deposited layer was composed of body-centred cubic (BCC) peaks ($2\theta = 44.5°$, 64.6°, and 81.9°). However, a low-intensity FCC peak ($2\theta = 43.5°$) was observed owing to the FCC phase formed by the dilution of the Ni composition in the Fe–Cr–Si deposited specimen. Based on these results, it can be predicted that a small amount of austenite phase transformation probably occurred because of the Ni dilution.

Fig. 5 shows the line component analysis of the specimens deposited using the STS 316 L and Fe–Cr–Si powders acquired through EPMA. The EPMA line analysis was performed along the blue line from the upper regions of the second deposited layer to some areas of the substrate, as shown in Fig. 3. The STS 316 L powder is mainly composed of various alloy components, such as Fe, Cr, Ni, Mo, and Si, whereas the Fe–Cr–Si powder is composed of Fe, Cr, and Si components. Therefore, the component behavior of each deposited specimen was confirmed by the main components, such as Fe, Cr, Ni, and Si. The Fe, Cr, Ni, and Si components between the deposited layer and substrate showed similar behavior in the STS 316 L specimen, whereas in the Fe–Cr–Si specimen, each component appeared to show an irregular cycle from the interface of the deposited layer and substrate to the specific upper area (first layer). A clear distinction between each deposited layer in the Fe–Cr–Si specimen was possible because the Ni component of the substrate was diluted in the first deposited layer during additive manufacturing. The region showing a sharp difference in the Fe, Cr, and Ni components in the first deposited layer of the Fe–Cr–Si specimen was similar to the white and black bands in the lower region of the first layer in Fig. 3b. In the white/black bands in Fig. 3b, it can be seen that Ni-rich and Ni-depleted regions coexist.

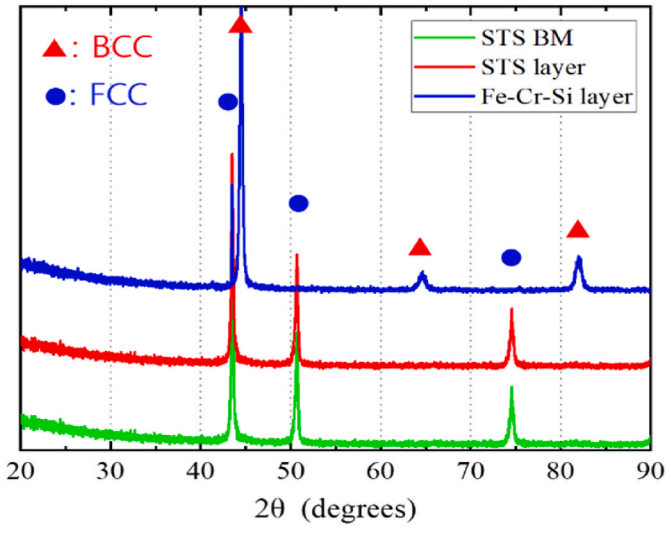

Fig. 4. Crystal structure acquired through X-ray diffraction patterns of deposited layers produced using stainless steel 316 L and Fe–Cr–Si powders.

EPMA-based mapping was performed to confirm the component behavior of each deposited specimen. The segregation behavior of the Ni component was representatively indicated to ensure the reliability of the preceding line analysis (Fig. 5), as shown in Fig. 6. As the powder composition was similar to that of the substrate, there was no noticeable dilution region of Ni or other components in the STS 316 L specimen. However, because the Fe–Cr–Si specimen showed a significant difference between the powder composition and that of the substrate, the Ni component of the substrate was clearly diluted in the deposited layer, as shown in Fig. 6b. The segregation rate of Ni was high in the first layer close to the substrate, and the ratio of the Ni component significantly decreased in the second layer, as shown in Fig. 5b. This is because, in the second deposited layer, only the Ni component segregated from the first layer was diluted; thus, the ratio was inevitably reduced. The region of the black/white band (Fig. 3b), and the region, in which the period of each component in the first deposited layer (Fig. 5b), showed a sharp difference were the same as those indicated by the white dotted box in Fig. 6b. Therefore, the black band represents the region where the segregation of the Ni component is low, and the white band represents the region where the segregation rate of Ni is high. It can be seen that various components are extremely diluted at the interface between the substrate of the Fe–Cr–Si specimen and first deposited layer, and it must be considered that a phase transformation may occur in the deposited layer because of this phenomenon.

Fig. 7 shows the microstructure and phase transformation behavior acquired by the IPF and phase map of the EBSD in the layers deposited using the STS 316 L and Fe–Cr–Si powders. A phase transformation behavior analysis was performed from the upper region of the second deposited layer to the area containing part of the substrate along the area indicated by the red dotted line, as shown in Fig. 6. Because the powder composition was similar to that of the substrate, both the substrate and deposited layer were FCC in the STS 316 L specimen. As mentioned in the Materials and Methods section, the second layer was deposited through 90° rotation, considering the coarsening of the columnar grains of the second layer because the cooling rate became slower toward the top of the deposited layer. The fact that the deposition direction of the second layer was rotated by 90° can be observed from the grain growth direction because the coarse columnar grains of the second layer showed an elongated shape along the deposition direction.

This phenomenon can also be explained using the kernel average misorientation (KAM) map from the EBSD. The dislocation density of the grains in the first layer was higher than that of the coarse grains in the second layer because the fine columnar grains in the first layer grew at a higher cooling rate. Conversely, in the Fe–Cr–Si specimen, the substrate and deposited layer were the FCC and BCC, respectively. As shown in Fig. 5b, in the Fe–Cr–Si specimen, the Ni component of the substrate was diluted with the first layer during the buildup of the first deposited layer. During this process, an unmixed zone was formed where the powder was incompletely mixed with the substrate, mainly at the interface between the substrate and first deposited layer with an extreme dilution of composition, and was composed of the FCC phase. In our previous research, when Fe–Cr–Si powder was deposited on a substrate mainly composed of austenite, an unmixed zone was generated at the interface between the substrate and deposited layer [27]. The created unmixed zone remains FCC; in the case of a small amount of diluted Ni component, it becomes a martensite nucleation site and participates in the martensite phase transformation. Dense martensite was mainly formed in the first layer because of the large amount of Ni dilution in the first layer and deformation owing to the build-up of the second layer. The Ni dilution rate of the second deposited layer is lower than that of the first layer, as shown in Fig. 6b. Therefore, several primary δ-ferrites were observed in the second layer. Primary δ-ferrites and martensite can also be distinguished on the KAM map. In general, martensite has a higher dislocation density; therefore, it has a lighter colour range than the

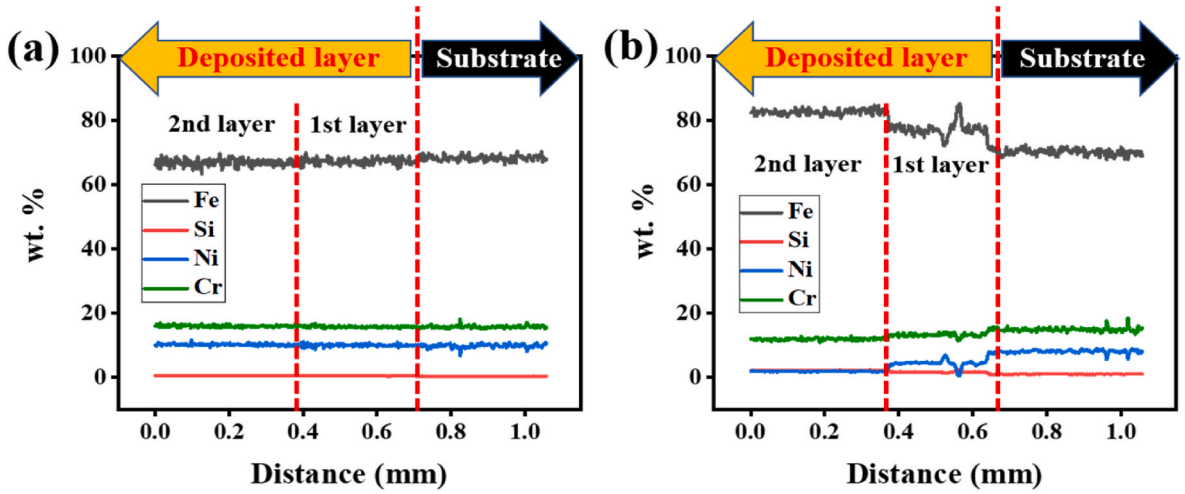

Fig. 5. Component behavior of deposited layers produced using: (a) stainless steel 316 L and (b) Fe–Cr–Si powder.

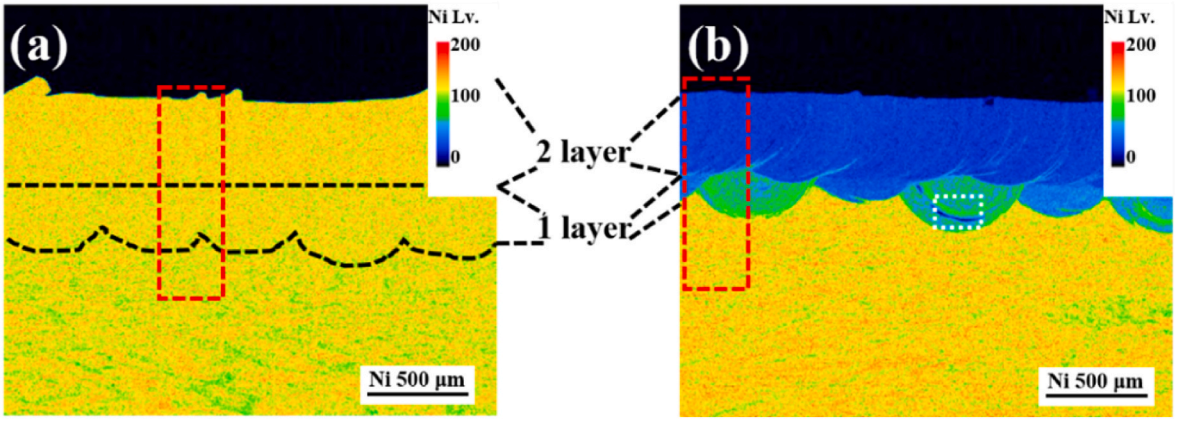

Fig. 6. Ni segregation of deposited layers produced using various powders: (a) stainless steel 316 L, and (b) Fe–Cr–Si powders.

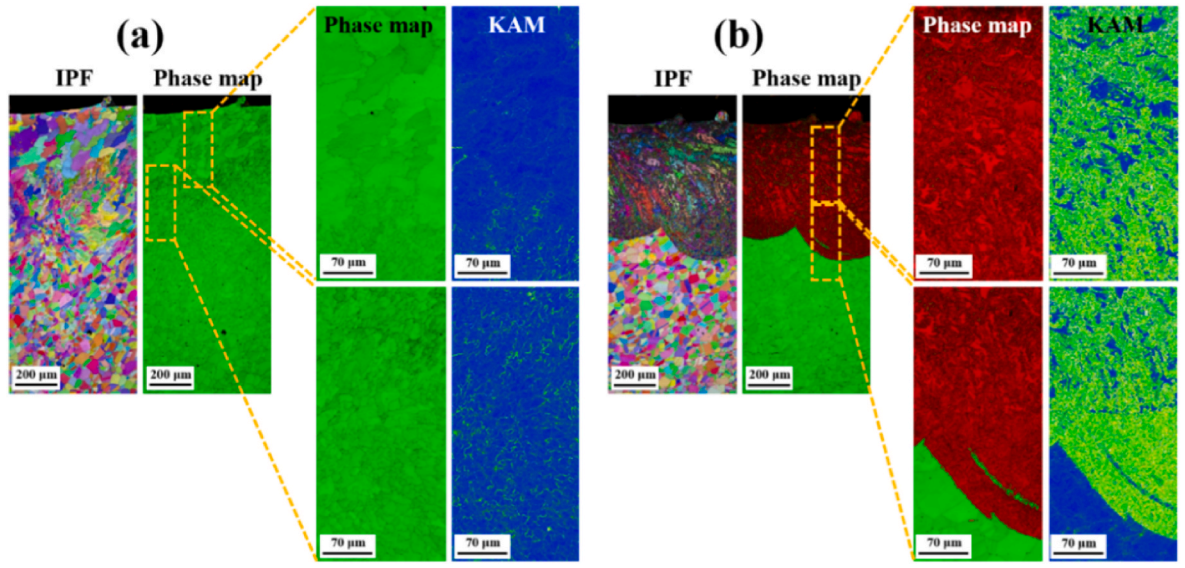

Fig. 7. Phase transformation behavior of deposited layers produced using: (a) stainless steel 316 L, and (b) Fe–Cr–Si powders.

primary δ-ferrite. The mechanical and corrosion properties differ depending on the major microstructures of the deposited layers in each specimen.

Fig. 8 shows the hardness measurement area and hardness distribution of the specimens deposited using the STS 316 L and Fe–Cr–Si powders. The average hardness of the STS 316 L used as a substrate was

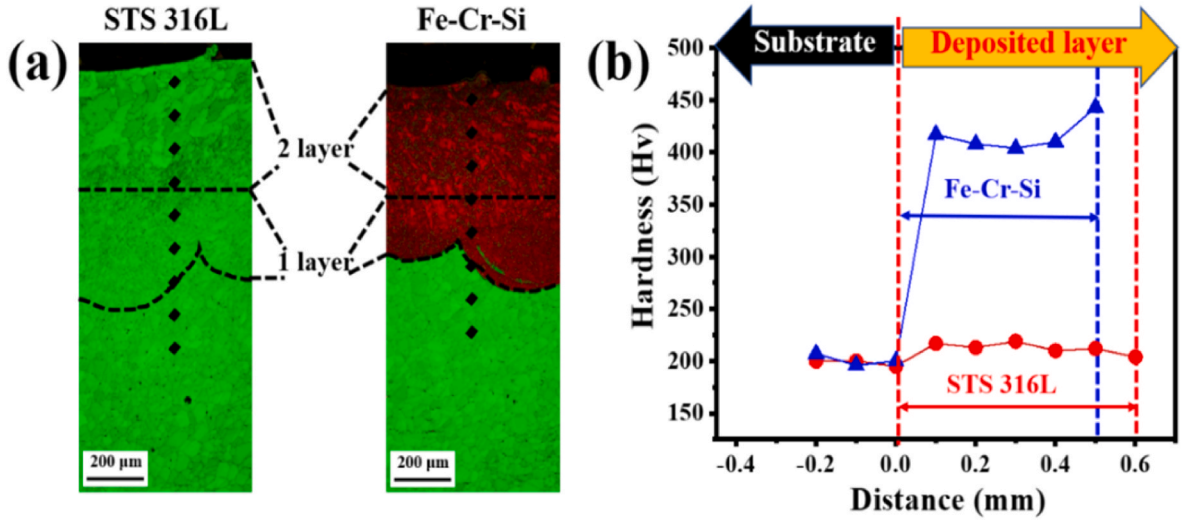

Fig. 8. Hardness behavior of deposited layers produced using stainless steel 316 L and Fe–Cr–Si powders: (a) hardness measurement area and (b) hardness distribution in deposited specimens.

approximately 210 ± 2 $Hv_{0.2}$, and it decreased to approximately 200 ± 1 $Hv_{0.2}$ in the region close to the boundary between the substrate and deposited layer. This was because most of the coarse grains in the heat-affected zone (HAZ) generated by cladding heat were included. However, in the deposited layer of each specimen, the hardness distribution differed significantly depending on the main phase (FCC or BCC). The hardness of the first layer with fine columnar grains was approximately 8 $Hv_{0.2}$ higher than that of the second layer with coarse equiaxed grains in the STS 316 L specimen. The deposited layer of the Fe–Cr–Si specimen showed the highest hardness values of 433 ± 1 and 420 ± 1 $Hv_{0.2}$ in the upper part of the second and first layers, respectively. This is because a large amount of dense martensite is formed in the upper and lower regions of the deposited layer. Because the main phases of each deposited layer are clearly divided into austenite and martensite, the corrosion characteristics may differ depending on the main phases.

4. Corrosion behavior of each clad

Fig. 9 shows the potentiodynamic polarisation test results, which were conducted in a 0.5 M H_2SO_4 solution of STS 316 L and Fe–Cr–Si deposited specimens; the Tafel fitting results are listed in Table 2. Both

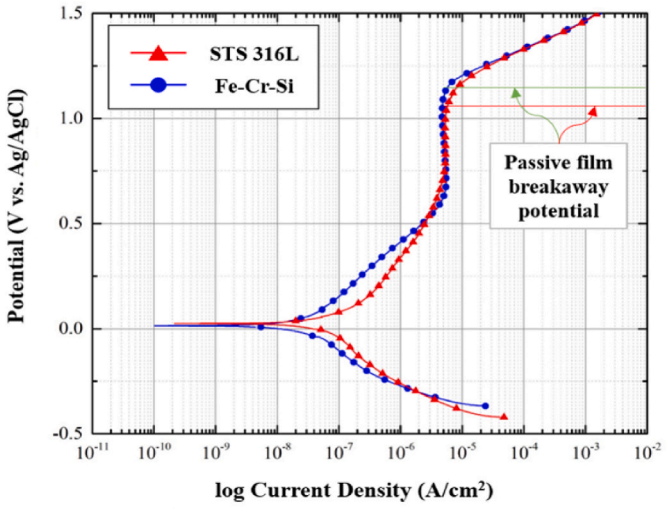

Fig. 9. Polarisation curves for each deposited layer produced using stainless steel 316 L and Fe–Cr–Si powders.

Table 2
Tafel fitting parameters of potentiodynamic polarisation test results.

Deposited layer	E_{corr} (mV vs. Ag/AgCl)	I_{corr} (nA/cm^2)	Corrosion rate (mm/yr)
stainless steel 316 L	24.4	111.0	0.051
Fe–Cr–Si	14.6	38.2	0.017

the STS 316 L and Fe–Cr–Si deposited layers showed similar corrosion potential (E_{corr}) of 24.4 mV and 14.6 mV, respectively. However, the corrosion current density (i_{corr}) of the Fe–Cr–Si-deposited specimen was significantly lower than that of the STS 316 L specimen. The i_{corr} value of the Fe–Cr–Si specimen was 38.2 nA/cm^2, whereas that of the STS 316 L specimen was 111.0 nA/cm^2. Using Faraday's law, i_{corr} can be converted to the corrosion rate, and the Fe–Cr–Si deposited layer was found to have a significantly lower corrosion rate than the STS 316 L layer. This is probably owing to the formation of oxide films, such as Cr_2O_3 and SiO_2 in the Fe–Cr–Si deposited layer. In the passive region (Potential >0.5 V vs. Ag/AgCl), each cladding exhibited a similar passive current density; however, the breakaway potential of the Fe–Cr–Si deposited layer was higher than that of the STS 316 L layer. This explains the reasons for the passive films formed on the Fe–Cr–Si deposited layer being more stable than those formed on the STS 316 L layer.

5. Mechanical properties of each clad

Fig. 10 shows the tensile behavior at room temperature (RT), 300, and 600 °C of the deposited specimens using the STS 316 L and Fe–Cr–Si powders. The tensile test temperature was similar to that of the high-temperature environment of current nuclear power plants. The high-temperature tensile specimens were extracted from the deposited specimens of each powder. In the STS 316 L deposited specimen, as the temperature of the high-temperature tensile test increased from RT to 600 °C, the yield strength (YS) and tensile strength (TS) decreased from 520 to 430 MPa and from 665 to 517 MPa, respectively. However, the elongation (E_f) increased from 23.7 to 31.8 %. This trend in the STS 316 L deposited specimen was consistent with the general high-temperature tensile behavior results. However, because the Fe–Cr–Si-deposited specimen was mainly composed of ferrite and martensite with a BCC structure, its high-temperature tensile behavior was expected to differ from that of the STS 316 L specimen. For Fe–Cr–Si specimens, YS and TS decreased from 681 to 260 MPa and 857 to 327 MPa, respectively, as the

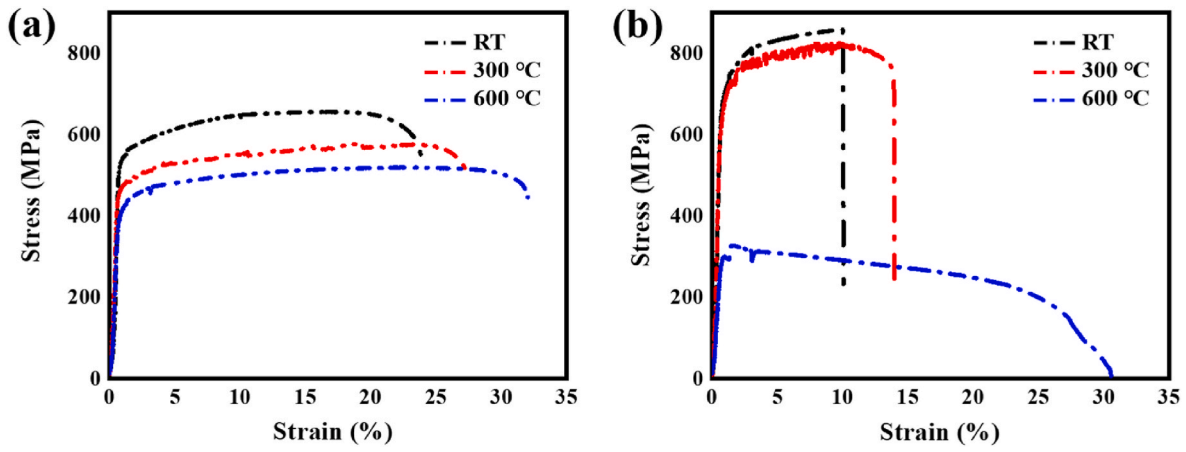

Fig. 10. Tensile properties of deposited specimens tested at RT, 300, and 600 °C: (a) stainless steel 316 L and (b) Fe–Cr–Si.

temperature of the high-temperature tensile test increased from RT to 600 °C. Nevertheless, the E_f increased from 10.1 to 30.5 %. This trend in the Fe–Cr–Si specimen is consistent with the general high-temperature tensile behavior results. The strength of the Fe–Cr–Si specimen increased, but the elongation decreased at RT and 300 °C compared to the STS 316 L specimen owing to the differences in the main microstructures. However, the strength and elongation were similar to those of the STS 316 L specimen at 600 °C. These results indicate that the Fe–Cr–Si specimen can undergo phase transformation during high-temperature tensile testing at 600 °C.

To understand the mechanism of high-temperature tensile properties of each deposited specimen at 600 °C, Fig. 11 shows the microstructure near the tensile fracture of the STS 316 L and Fe–Cr–Si deposited specimens. The microstructures were analysed through EBSD using the IPF, KAM, and phase maps. Through KAM, the change in the dislocation density according to the strain formed by the high-temperature tensile test was confirmed, and phase identification was conducted to measure austenite and $Cr_{23}C_6$ (red), α′-martensite and ferrite (green), and Cr_7C_3 (yellow) using a phase map.

At 600 °C, the fracture areas of all the tensile specimens were significantly deformed. As shown in Fig. 7a, the STS 316 L layer deposited at RT exhibited an FCC phase with a minimal formation of Cr-rich carbides. However, after experiencing high-temperature tensile stress at 600 °C, the formation rate of Cr-rich carbides was higher than that at RT. Despite the high-temperature tensile specimens having the same STS 316 L deposited layer, it was confirmed that the fractions of Cr-rich carbides and ferrites changed with strain. The dislocation density was high at the grain boundaries in the region where deformation began owing to the tensile stress, and Cr-rich carbides were generated in the same region in the phase map. Generally, in Fe–Cr alloys, fine Cr-rich particles are formed along the grain boundaries, and the presence of these particles hinders the movement of dislocations during plastic deformation, thereby contributing to tensile strength [32–34]. Approaching the fracture region, the fractions of Cr-rich carbide and ferrite were 18.5 and 2.5 % higher, respectively, than those in the region where deformation began because the dislocation density was higher overall and at the grain boundaries.

This phenomenon also occurred in the Fe–Cr–Si deposited specimen. In the high-temperature tensile specimen at 600 °C, the Cr-rich carbide fraction (15 %) near the fracture region showed a 3 % higher result than

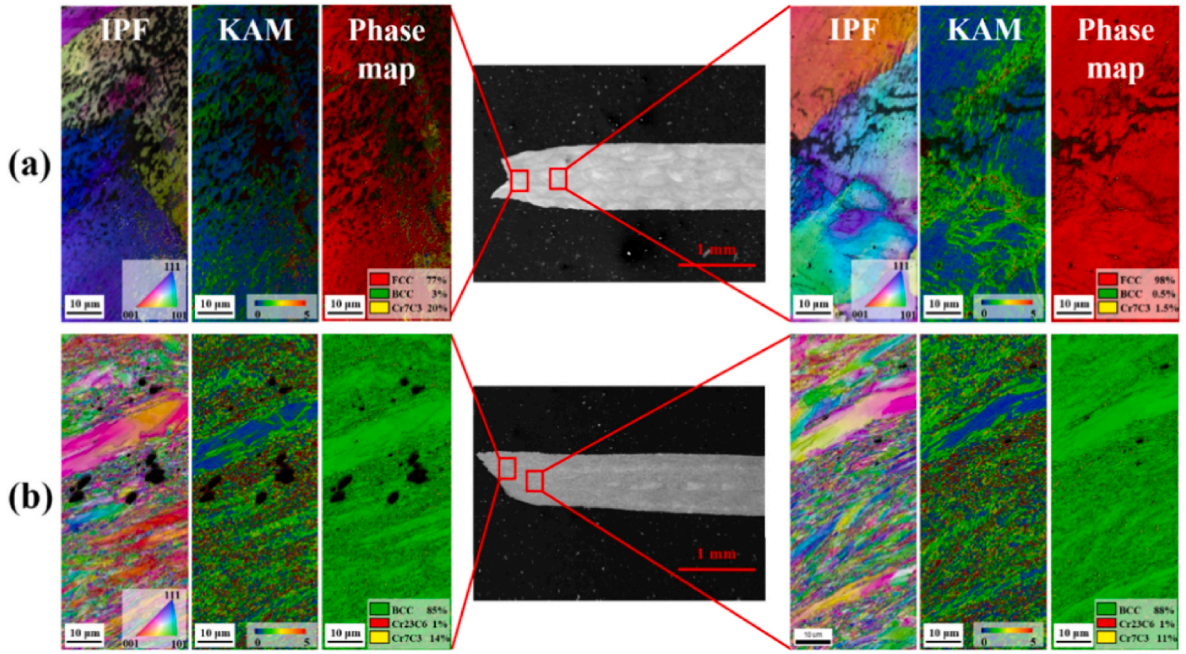

Fig. 11. Microstructures near the tensile fracture location tested at 600 °C in each deposited specimen: (a) stainless steel 316 L, and (b) Fe–Cr–Si.

that in the region where the deformation began (12 %). Martensitic STS is composed of ferrite and Cr-rich carbide structures during heat treatment at 600 °C [14,15]. After a high-temperature tensile test at 600 °C, the tensile strength of the Fe–Cr–Si deposited specimens decreased rapidly, and the elongation increased because the temperature and applied strain caused the phase transformation and formation of the carbides. Because the Cr-rich carbide fraction in the fracture region of all the high-temperature tensile specimens was higher than that in the region where deformation began, the effect of strain on the formation of carbides may have been an important factor.

Fig. 12 shows the fracture-surface morphologies of the deposited specimens using the STS 316 L and Fe–Cr–Si powders at 600 °C. The fracture surface of the STS 316 L deposited specimen exhibited a dimpled morphology, which is characteristic of ductile fracture, as shown in Fig. 12a. However, localised quasi-cleavage (QC) was also observed in the central area of the fracture surface. This result is probably because there is an area where the phase transformation and formation of carbides are concentrated in the central area near the fracture position in the STS 316 L deposited specimen. In contrast, the fracture surfaces of the Fe–Cr–Si deposited specimens were mostly brittle. Most of the fracture surfaces exhibited a cleavage shape, and the brittle fracture results were significantly influenced by the main microstructure of the deposited specimen.

This trend in the STS 316 L and Fe–Cr–Si deposited specimens was consistent with the general high-temperature tensile behavior results. However, in the high-temperature tensile results at 600 °C, the strength decreased, and the elongation tended to increase owing to the density of carbides and occurrence of phase transformation. It was confirmed that the strength and elongation changed significantly in the Fe–Cr–Si specimens, mainly because the main phase changed from martensite to ferrite. Considering these problems, it is assumed that Fe–Cr–Si materials can also be used as coating materials for pipes because the pipes of nuclear power plants are mainly operated at temperatures below 600 °C.

To improve the high-temperature properties and corrosion resistance of the Fe–Cr–Si deposited layer produced through laser DED, we not only observed the mechanical properties and corrosion characteristics of the Fe–Cr–Si deposited specimen according to the heat input but also observed the corrosion resistance at high temperatures in the LBE environment. Future research should confirm whether these technologies can be applied to nuclear power plant piping systems.

6. Conclusions

In this study, a laser DED process was used to produce corrosion-resistant layers on an STS 316 L substrate using STS 316 L and Fe–Cr–Si alloy powder. Based on the study of the microstructures, corrosion, and mechanical properties of each deposited specimen manufactured by the additive manufacturing at RT, 300, and 600 °C, the following conclusions can be drawn:

1) Sound-deposited layers without defects were obtained from all the specimens. In the STS 316 L deposited specimen, both the substrate and deposition layer were composed of the FCC phase, whereas the deposited layer in the Fe–Cr–Si deposited specimen was distinctly separated from the substrate because it was composed of the BCC phase.
2) Because the average hardness of the 316 L deposited layer was approximately 210 Hv, the austenite was similar to that of the substrate, and the average hardness of the Fe–Cr–Si deposited layer was approximately 420 Hv, which was mainly composed of martensite.
3) Despite its phase differences, the Fe–Cr–Si deposited layer surface showed a lower corrosion rate than the STS 316 L deposited layer.
4) In the high-temperature tensile test of the Fe–Cr–Si deposited specimen at 600 °C, the strength decreased and the elongation was increased, owing to the density of carbides and occurrence of phase transformation.
5) Surface coatings made from Fe–Cr–Si materials are suitable for nuclear power plant piping systems mainly operating below 600 °C.
6) The Fe–Cr–Si layer deposited with the laser DED process can be applied to the fourth generation nuclear power generation system using an LBE, and its scope of application can be expanded to various industries requiring high-temperature corrosion performance.

CRediT authorship contribution statement

Gidong Kim: Investigation, Methodology, Formal analysis, and writing - original draft. **Hyunbin Nam**: Investigation, Methodology, Formal analysis, and writing - original draft. **Taewoo Hwang**: Investigation, Resources. **Seunghyun Kim**: Investigation, Formal analysis, and resources. **Ji Hyun Kim**: Supervision, conceptualisation, writing, review, and editing. **Sangwoo Song**: Supervision, Writing - review and editing, and funding acquisition.

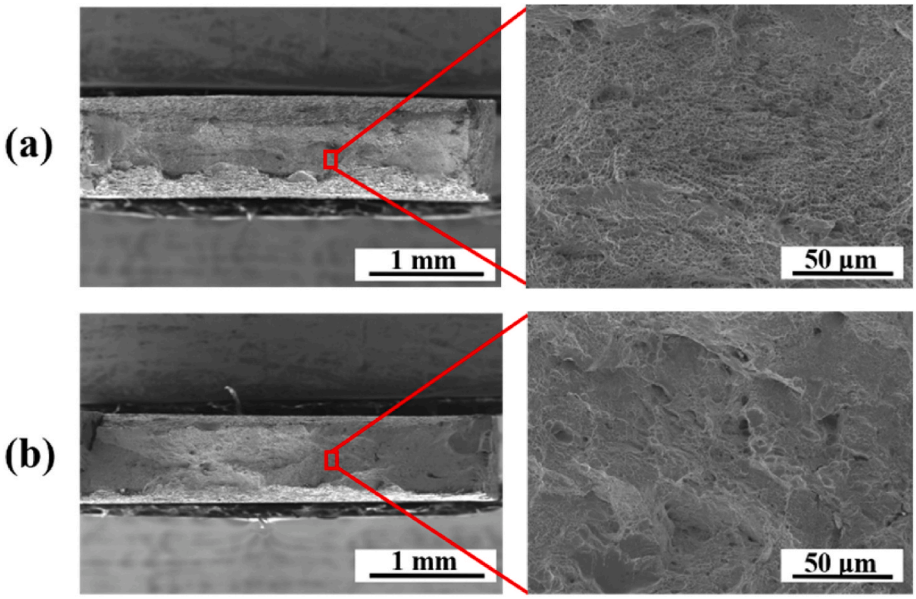

Fig. 12. Fracture-surface morphologies of deposited specimens tested at 600 °C: (a) stainless steel 316 L, and (b) Fe–Cr–Si.

Data availability

No data was used for the research described in the article.

Declaration of competing interest

The authors declare the following financial interests/personal relationships which may be considered as potential competing interests: Sangwoo Song reports financial support was provided by Korea Institute of Materials Science. If there are other authors, they declare that they have no known competing financial interests or personal relationships that could have appeared to influence the work reported in this paper.

Acknowledgements

This study was supported by the Fundamental Research Program of the Korea Institute of Material Science (KIMS) (Grant No. PNK 8880), and the Korea Institute of Energy Technology Evaluation and Planning (KETEP) and the Ministry of Trade, Industry & Energy (MOTIE) of the Republic of Korea (No. RS-2023-00240918).

References

[1] Xiao Q, Jang C, Kim C, Chen J, Jeong C, Kim SH. Corrosion behavior of Fe-based candidate accident tolerant fuel cladding alloys in spent fuel pool environment – effect of prior corrosion. J Nucl Mater 2021;548:152845. https://doi.org/10.1016/j.jnucmat.2021.152845.

[2] Qiang R, Leong A, Zhang J, Short MP. Corrosion behavior of Fe–Cr–Si alloys in simulated PWR primary water environment. J Nucl Mater 2019;526:151735. https://doi.org/10.1016/j.jnucmat.2019.07.035.

[3] Chao Q, Cruz V, Thomas S, Birbilis N, Collins P, Taylor A, Hodgson PD, Fabijanic D. On the enhanced corrosion resistance of a selective laser melted austenitic stainless steel. Scripta Mater 2017;141:94–8. https://doi.org/10.1016/j.scriptamat.2017.07.037.

[4] Liu Y, Liu L, Li S, Wang R, Guo P, Wang A, Ke P. Accelerated deterioration mechanism of 316L stainless steel in NaCl solution under the intermittent tribocorrosion process. J Mater Sci Technol 2022;121:67–79. https://doi.org/10.1016/j.jmst.2022.01.011.

[5] Satheesh Kumar SS, Vasanth M, Singh V, Ghosal P, Raghu T. An investigation of microstructural evolution in 304L austenitic stainless steel warm deformed by cyclic channel die compression. J Alloys Compd 2017;699:1036–48. https://doi.org/10.1016/j.jallcom.2016.12.321.

[6] Zhou Y, Liu Y, Zhou X, Liu C, Yu J, Huang Y, Li H, Li W. Precipitation and hot deformation behavior of austenitic heat-resistant steels: a review. J Mater Sci Technol 2017;33:1448–56. https://doi.org/10.1016/j.jmst.2017.01.025.

[7] Li H, Zhang B, Jiang Z, Zhang S, Feng H, Han P, Dong N, Zhang W, Li G, Fan G, Lin Q. A new insight into high-temperature oxidation mechanism of super-austenitic stainless steel S32654 in air. J Alloys Compd 2016;686:326–38. https://doi.org/10.1016/j.jallcom.2016.06.023.

[8] Park G, Hong S, Yeau K, Jeong B. T-joint fillet laser welding of high-strength stainless steel for curtain wall frames. J Weld Join 2022;40:485–95. https://doi.org/10.5781/JWJ.2022.40.6.4.

[9] Huang X, Xiao K, Fang X, Xiong Z, Wei L, Zhu P, Li X. Oxidation behavior of 316L austenitic stainless steel in high temperature air with long-term exposure. Mater Res Express 2020;7:066517. https://doi.org/10.1088/2053-1591/ab96fa.

[10] Jozaghi T, Samimi P, Chumlyakov Y, Karaman I. Role of thermally stable deformation twins on the high-temperature mechanical response of an austenitic stainless steel. Mater Sci Eng A 2022;845:143199. https://doi.org/10.1016/j.msea.2022.143199.

[11] Yi MS. Comparison of welding deformation characteristics by circumferential welding for austenitic and duplex stainless steel pipe: experimental study. J Weld Join 2022;40:141–8. https://doi.org/10.5781/JWJ.2022.40.2.5.

[12] Jeong EH, Kim JH, Kim SH, Kim YD. Creep rupture characteristics of cladding tubes of FC92B and FC92N: candidate alloys of SFR fuel cladding tube materials. Met Mater Int 2022;28:1445–54. https://doi.org/10.1007/s12540-021-01031-5.

[13] Zala AB, Jamnapara NI, Badheka VJ, Sasmal C, Sam S, Ranjan M. Delta (δ) ferrite formation in the welds of aluminized 9Cr-1Mo steels. Metallogr Microstruct Anal 2019;8:256–62. https://doi.org/10.1007/s13632-019-00528-1.

[14] Jeong EH, Kim JH, Kim SH, Kim YD. Effect of boron on the thermal stability of the precipitate phase of FC92B and FC92N steels during aging and creep. Met Mater Int 2021;27:985–94. https://doi.org/10.1007/s12540-019-00473-2.

[15] Jiang G, Xu D, Feng P, Guo S, Yang J, Li Y. Corrosion of FeCrAl alloys used as fuel cladding in nuclear reactors. J Alloys Compd 2021;869:159235. https://doi.org/10.1016/j.jallcom.2021.159235.

[16] Küchler S, Vojtech V, Gerstl SSA, Schäublin RE, Löffler JF. Thermally decomposed binary Fe-Cr alloys: toward a quantitative relationship between strength and structure. Adv Eng Mater 2022;24:2100909. https://doi.org/10.1002/adem.202100909.

[17] Matijasevic M, Almazouzi A. Effect of Cr on the mechanical properties and microstructure of Fe-Cr model alloys after n-irradiation. J Nucl Mater 2008;377:147–54. https://doi.org/10.1016/j.jnucmat.2008.02.061.

[18] Lee EH, Yu CJ, Lee HB, Kim JH, Suh DW. Influence of Si and Al contents and isothermal treatment condition on the microstructure and tensile properties in ultra-high strength Fe-0.2C-2.0Mn martensite-bainite complex phase steels. Kor J Met Mater 2021;59:602–12. https://doi.org/10.3365/KJMM.2021.59.9.602.

[19] Kuksenko V, Pareige C, Genevois C, Pareige P. Characterisation of Cr, Si and P distribution at dislocations and grain-boundaries in neutron irradiated Fe-Cr model alloys of low purity. J Nucl Mater 2013;434:49–55. https://doi.org/10.1016/j.jnucmat.2012.11.027.

[20] Lu Z, Faulkner RG, Was G, Wirth BD. Irradiation-induced grain boundary chromium microchemistry in high alloy ferritic steels. Scripta Mater 2008;58:878–81. https://doi.org/10.1016/j.scriptamat.2008.01.004.

[21] Paul S, Muralles M, Schwen D, Short M, Momeni K. A modified embedded-atom potential for Fe-Cr-Si alloys. J Phys Chem C 2021;125:22863–71. https://doi.org/10.1021/acs.jpcc.1c07021.

[22] Qiang R, Leong A, Zhang J, Short MP. Corrosion behavior of Fe–Cr–Si alloys in simulated PWR primary water environment. J Nucl Mater 2019;526:151735. https://doi.org/10.1016/j.jnucmat.2019.07.035.

[23] Moon J, Kim S, Park WD, Kim TY, McAlpine SW, Short MP, Kim JH, Bahn CB. Initial oxidation behavior of Fe-Cr-Si alloys in 1200 °C steam. J Nucl Mater 2019;513:297–308. https://doi.org/10.1016/j.jnucmat.2018.10.010.

[24] Qiang R, Leong A, Zhang J, Short MP. Corrosion behavior of Fe-Cr-Si alloys in simulated PWR primary water environment. J Nucl Mater 2019;526:151735. https://doi.org/10.1016/j.jnucmat.2019.07.035.

[25] Idczak K, Idczak R. Investigation of surface segregation in Fe-Cr-Si alloys by XPS. Metall Mater Trans A 2020;51:3076–89. https://doi.org/10.1007/s11661-020-05758-5.

[26] Xu Z, Song L, Zhao Y, Liu S. The formation mechanism and effect of amorphous SiO2 on the corrosion behaviour of Fe-Cr-Si ODS alloy in LBE at 550 °C. Corrosion Sci 2021;190:109634. https://doi.org/10.1016/j.corsci.2021.109634.

[27] Hwang T, Kim GD, Kim SW, Moon YH, Nam H, Song S. Effect of laser traverse speed on the metallurgical properties of Fe-Cr-Si clads for austenitic stainless steel using directed energy deposition. Crystals 2022;12:1531. https://doi.org/10.3390/cryst12111531.

[28] Bamba G, Wouters Y, Galerie A, Charlot F, Dellali A. Thermal oxidation kinetics and oxide scale adhesion of Fe–15Cr alloys as a function of their silicon content. Acta Mater 2006;54:3917–22. https://doi.org/10.1016/j.actamat.2006.04.023.

[29] Short MP, Ballinger RG, Hänninen HE. Corrosion resistance of alloys F91 and Fe–12Cr–2Si in lead–bismuth eutectic up to 715 °C. J Nucl Mater 2013;434:259–81. https://doi.org/10.1016/j.jnucmat.2012.11.010.

[30] Thompson SM, Bian L, Shamsaei N, Yadollahi A. An overview of Direct Laser Deposition for additive manufacturing; PartI: transport phenomena, modeling and diagnostics. Addit Manuf 2015;8:36–62. https://doi.org/10.1016/j.addma.2015.07.001.

[31] Singh A, Kapil S, Das M. A comprehensive review of the methods and mechanisms for powder feedstock handling in directed energy deposition. Addit Manuf 2020;35:101388. https://doi.org/10.1016/j.addma.2020.101388.

[32] Akhtar M, Khajuria A. The synergistic effects among crystal orientations, creep parameters, local strain, macro–microdeformation, and polycrystals' hardness of boron alloyed P91 steels, steel. Res Intell 2022;93:2100819. https://doi.org/10.1002/srin.202100819.

[33] Khajuria A, Shiva S, Misra A. The carbon content effect on hot-rolled C–Mn micro-alloyed E410 structural steel. Vacuum 2023;212:112042. https://doi.org/10.1016/j.vacuum.2023.112042.

[34] Akhtar M, Khajuria A. The synergistic effects of boron and impression creep testing during paced controlling of temperature for P91 steels. Adv Eng Mater 2023;25:3200053. https://doi.org/10.1002/adem.2023000053.